Available online at www.sciencedirect.com
ScienceDirect
International Journal of Heat and Mass Transfer 50 (2007) 687–701
International Journal of HEAT and MASS TRANSFER
www.elsevier.com/locate/ijhmt

Analysis of chemical-reaction-coupled mass and heat transport phenomena in a methane reformer duct for PEMFCs

Jinliang Yuan [a], Fuan Ren [b], Bengt Sundén [a,*]

[a] Department of Energy Sciences, Faculty of Engineering, Lund University, Box 118, 22100 Lund, Sweden
[b] Marine Engineering College, Dalian Maritime University, Dalian 116026, China

Received 25 April 2006
Available online 15 September 2006

Abstract

Mass, heat and momentum transport processes are coupled with catalytic chemical reactions in a methane steam reforming duct. It is often found that endothermic and exothermic reactions in the ducts are strongly integrated by heat transfer from adjacent catalytic combustion ducts. In this paper, a three-dimensional calculation method is developed to simulate and analyze reforming reactions of methane, and the effects on various transport processes in a steam reforming duct. The reformer conditions such as mass balances associated with the reforming reactions and gas permeation to/from the porous catalyst reforming layer are applied in the analysis. The predicted results are presented and discussed for a composite duct consisting of a porous catalyst reaction layer, the fuel gas flow duct and solid layers. Parametric studies are conducted to reveal the importance of reformer designs and operating conditions. The results show that the variables, such as porous layer configuration, temperature and catalyst loading, have significant effects on the transport processes and reformer performance.

Keywords: Transport phenomena; Reaction; Analysis; Reformer duct; PEMFCs

1. Introduction

In general, low temperature fuel cells (such as proton exchange membrane fuel cells – PEMFCs hereafter) essentially need pure hydrogen to be supplied to the anodes of the stacks. However, hydrogen does not appear naturally as a gaseous fuel, and it usually has to be generated from whatever fuel source is locally available. For this case, external fuel reformers/processors should be incorporated into the PEMFC systems. Methane is a convenient feedstock because the existing natural gas pipeline infrastructure makes it readily available and accessible at any point along the distribution chain. Availability of highly compact hydrogen generators will make possible electrical power generation by PEMFCs at central stations, substations, or residences.

Methane is usually converted into H_2, CO and CO_2 by employing Ni as a catalyst supported by alumina in the reformers. Such reformers have been developed in last years. In general, technologies to produce hydrogen from methane are based on one of the following processes: steam methane reforming (SMR), partial oxidation (POX) and autothermal reforming (ATR). SMR has been extensively studied and is the most common and traditional method for producing hydrogen on an industrial scale. In this process, steam reacts with methane to produce hydrogen, carbon dioxide and carbon monoxide in catalyst reformers. It should be mentioned that the steam reforming process is strongly endothermic and needs external heat to be supplied through the reactor wall. Consequently the overall SMR configurations with heat exchangers are very heavy [1]. However for PEMFCs, carbon monoxide is a poison that adversely affects its performance. The CO content must be reduced to below 10 ppm, see [2]. This is achieved by use of the water gas-shift reactions or even by

* Corresponding author. Tel.: +46 46 2228605; fax: +46 46 2224717.
E-mail address: bengt.sunden@vok.lth.se (B. Sundén).

0017-9310/$ - see front matter © 2006 Elsevier Ltd. All rights reserved.
doi:10.1016/j.ijheatmasstransfer.2006.07.005

Nomenclature

a	width of porous layer, m
b	width of flow duct, m
B	microscopic inertial coefficient, 1/m
D_h	hydraulic diameter, m
D_{hr}	hydraulic diameter ratio
c_p	specific heat capacity, J/(kg K)
D	diffusion coefficient of species, m^2/s
F	the Forchheimer coefficient
h	overall height of the duct, m; enthalpy, kJ/mol
h_d	height of the duct, m
h_p	thickness of porous catalytic layer, m
h_r	thickness ratio (h_p/h)
J	reaction related molar flux, mol/(m^2 s)
k	thermal conductivity, W/(m K); kinetic rate constant, kmol/(kg_{cat} h)
K_e	equilibrium constants, Pa^2
L	reformer length, m
m_{cl}	catalyst loading, kg_{cat}/m^3
$\dot{\mathbf{m}}$	mass diffusion flux, kg/(m^2 s)
$\dot{\mathbf{n}}$	molar diffusion flux, mol/(m^2 s)
M	molecular weight of species, kg/mol
P	pressure, Pa
PL_r	permeation length ratio
PR_r	permeation rate ratio
q	heat flux, W/(m^2)
R	reaction rate, kmol/(m^3 s)
$\Re$	gas constant, kJ/(mol K)
r_e	effective radius, m
Re	Reynolds number (UD_h/v)
S	source term
T	temperature, °C
$\mathbf{V}$	velocity vector, m/s
V_i	velocity components in x, y and z directions, respectively, m/s
x, y, z	Cartesian coordinates
X	molar fraction of fuel species
Y	mass fraction of fuel species

Greek symbols

β	permeability of porous layer, m^2
ε	porosity
μ	dynamic viscosity, kg/(m s)
v	kinematic viscosity, m^2/s
ρ	density, kg/m^3
τ	tortuosity

Superscripts

+	forward reaction
−	reverse reaction

Subscripts

di	diffusion
eff	effective parameter
f	fuel gas mixture
form	formation
gm	fuel gas mixture
CH_4	methane
CO	carbon monoxide
CO_2	carbon dioxide
H_2	hydrogen
H_2O	water
in	inlet
k	Knudsen diffusion
m	mass transfer
p	permeation
r	steam reforming reaction
re	reverse methanation reaction
s	solid wall; shift reaction

membrane separation techniques. To overcome the heat transfer problem in SMR, POX has been often employed because this process is exothermic and easily starts up even without the aid of a catalyst. The drawback is its high carbon monoxide fraction [1]. The exothermic and endothermic processes occur simultaneously in the ATR by feeding the fuel, water, and air together into the reactor. The thermal energy generated by POX is directly supplied to SMR, and hence the overall configuration is more compact and suitable for mobile fuel cells [1].

There is an increasing interest worldwide in the development of innovative fuel processing technologies for fuel cell systems, for instance, compact reformers (CR hereafter) for a variety of applications. The basic idea of the CR is, by applying thin coatings of catalyst, to catalytically activate both sides of a compact heat exchanger – one side for combustion to provide heat for the other side to sustain steam reforming of methane and produce hydrogen. In this configuration, the thin coating results in small thermal conduction and species diffusion path lengths that largely eliminate heat and mass transfer restrictions associated with conventional reformers, and an improved utilization of the intrinsic reforming catalyst kinetics is allowed to achieve an efficient transfer of thermal energy. The compact reformer concept and its potential high power density could lead to major applications in fuel cell systems for stationary and transportation applications [3,4]. For instance, coupling of steam reforming and catalytic combustion in adjacent ducts have received attention recently, and an excellent review can be found in [5] regarding the CR concept application and new design development. As revealed in [5,6], various aspects (functional catalyst, support material, reactor configuration/design, and operating conditions) have been investigated theoretically, mainly based on simplified one-

or two-dimensional approaches. Literature review shows that the research on the kinetic reaction performance and effects on the transport processes are very limited.

The objective of this study is to investigate various fundamental phenomena and parameter effects on the performance of a methane reforming duct, with the aims to provide improved understanding and to supply guidance for the practical implementation of such a design [7]. A three-dimensional computational procedure has been developed to simulate and analyse steam reforming of methane in a composite domain consisting of a porous active layer, a gas flow duct and solid plates. The reformer conditions such as the combined thermal boundary conditions (heat flux on the active solid wall and thermal insulation on the other solid walls), mass balances associated with the reforming reactions and gas permeation to/from the porous catalyst layer are applied in the analysis. Momentum and heat transport together with fuel gas species equations have been solved with coupled source terms and variable thermo-physical properties (such as density, viscosity, specific heat, etc.) of the fuel gas mixture.

2. Problem statement and motivation

There are several transport processes (such as mass, heat and momentum transport) together with chemical reactions appearing in multifunctional reactors. It is often found that the endothermic and exothermic reactions, such as hydrocarbon cracking, steam reforming and dehydrogenation, are strongly coupled by heat exchange in the reactors. There are three options for combining the endothermic process and the heat supplied by an exothermic reaction, as shown in Table 1.

There exist certain design challenges related to the in situ method, for instance, bifunctional catalysts are required to promote both endothermic and exothermic reactions in the same temperature range. For chronological segregation design, hot spots may appear in the active layers, and then damage the catalyst and the reactor material. Such problems can be addressed by spatial segregation of the endothermic and exothermic reactions by means of indirect heat exchange, see [5,6]. On the other hand, heat to keep the endothermic reaction can be supplied by use of

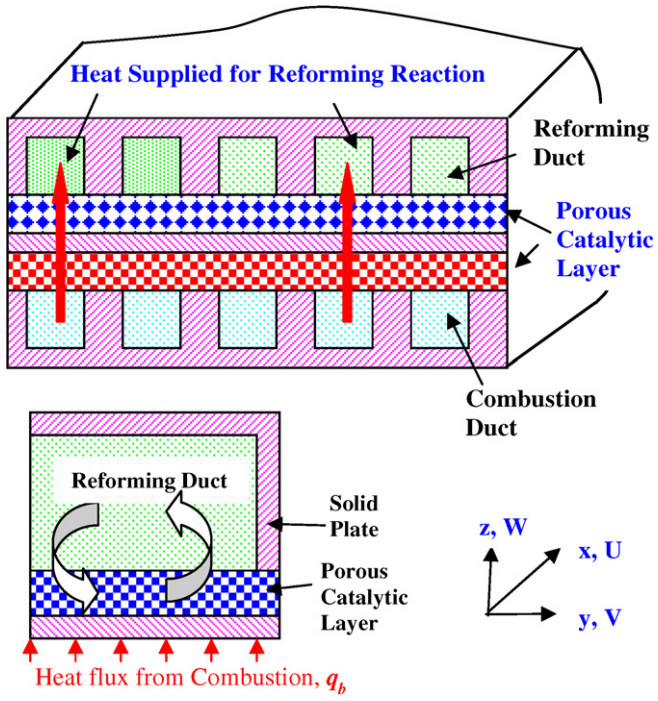

Fig. 1. Scheme of unit reactors (up); and an investigated duct of steam reforming reactors.

Table 1
Integration methods in reformers [5,6] (in the table, I – the endothermic process, II – the exothermic reaction)

Options	Integration methods
In situ heat generation via a couple reaction 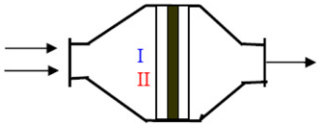	• Reactants for both reactions are mixed • All the reactions run in parallel • Direct heat transfer appears within the reacting mixture
Chronologically segregated heat generation, regenerative heat exchange 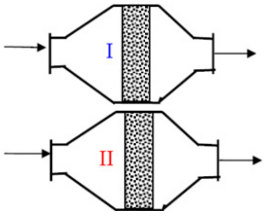	• The fixed bed is heated during the exothermic cycle • Stored heat is consumed in the endothermic process, and the fixed bed is cooled
Spatially segregated heat generation, recuperative heat exchange 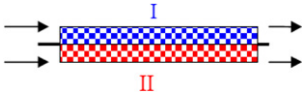	• Catalytic reactor is comprised of closely spaced and catalytically coated thin metal plates • Heat transfer resistances between reaction sites are effectively decreased

catalytic combustion at lower temperature than homogeneous combustion. Consequently, the spatial segregation design can reduce NO_x formation, and the channel dimensions can be scaled down to a few mm in the plate matrices, with an obvious impact on reformer size for the hydrogen generation unit near the site of use.

A three-dimensional computational fluid dynamics (CFD) code was used to simulate a methane reforming duct from a typical compact reformer, as shown in Fig. 1. The V_i is the velocity component in the x, y or z directions. In this study, the porous catalyst layer is assumed to be homogeneous and characterized by effective parameters and the fuel in the porous layer is in thermal equilibrium with the solid matrix. The reforming reactions take place within the porous catalyst layer. A constant flow rate $U = U_{in}$ with fixed mole fractions of the mixed fuel is specified at the inlet of the fuel flow duct, while $U = 0$ is specified at the inlet for the solid walls and the porous catalyst layer. Only half of the duct is considered by imposing symmetry conditions on the mid-plane, as shown in the lower diagram of Fig. 1.

3. Various processes and mathematical modelling

In a catalytic reformer, there are many reactions taking place. As revealed in [1,5,6], the steam reforming, water gas-shift, and reverse methanation reactions of methane are the major ones with significant reaction rates, while other side reactions include cracking of methane and carbon monoxide resulting in carbon deposition, and gasifying carbon by steam with very low reaction rates. Consequently, the above mentioned side reactions can be ignored, and only the following major chemical reactions are included in this study:

Methane steam reforming:

$$CH_4 + H_2O \rightarrow CO + 3H_2, \quad \Delta h_{(298\ K)} = 226,000\ kJ/kmol \tag{1}$$

Water gas-shift:

$$CO + H_2O \rightarrow CO_2 + H_2, \quad \Delta h_{(298\ K)} = -41,000\ kJ/kmol \tag{2}$$

Reverse methanation:

$$CH_4 + 2H_2O \rightarrow CO_2 + 4H_2, \quad \Delta h_{(298\ K)} = 165,000\ kJ/kmol \tag{3}$$

It should be mentioned that the above processes in Eqs. (1) and (3) are endothermic and the overall balance of the reactions requires net heat input. In general, this heat supply depends on the thermal integration methods employed and the associated combustion processes. In reality, its value is variable in both space and time, but is implemented by a constant heat flux q_b in this study. This limitation may be removed if the catalytic combustion processes are included in the adjacent combustion ducts.

The governing equations to be solved are the mass, momentum, energy and species conservation equations. The mass continuity equation is written as

$$\nabla \bullet (\rho_{eff}\mathbf{V}) = 0 \tag{4}$$

The momentum equation reads

$$\nabla \bullet (\rho_{eff}\mathbf{V}\mathbf{V}) = -\nabla P + \nabla \bullet (\mu_{eff}\nabla \mathbf{V}) + S_{di} \tag{5}$$

The inclusion of the source term S_{di} allows Eq. (5) to be valid for both the porous catalytic layer and the fuel gas flow duct

$$S_{di} = -(\mu_{eff}\mathbf{V}/\beta) - \rho_{eff}BV_i|\mathbf{V}| \tag{6}$$

The first term on the right-hand side of the above equation accounts for the linear relationship between the pressure gradient and flow rate according to Darcy's law. The second term is the Forchheimer term which takes into account the inertial force effects, i.e., the non-linear relationship between pressure drop and flow rate [8,9]. In Eq. (6), β is the porous layer permeability, and $\mathbf{V}$ represents the volume-averaged velocity vector of the species mixture. For example, the volume-averaged velocity component U in the x direction is equal to εU_p, where ε is the porosity and U_p is the average pore velocity (or interstitial velocity). The inertial coefficient B in the second term is an empirical function depending on the microstructure of the porous medium, e.g., $B = \varepsilon F/(\beta)^{0.5}$ employed in [8].

In the fuel (or gas) flow duct, the source term S_{di} becomes zero because the permeability β is infinite and B is zero. Eq. (5) then reduces to the regular Navier–Stokes equation. For the porous layer, the source term is not zero, and the momentum equation (5) with non-zero source term Eq. (6) can be regarded as a generalized Brinkman–Forchheimer-extended Darcy model. For more details, see [8] and the references included there. It accounts for the macroscopic inertial effects and shear stresses, and microscopic inertial effects as well.

Based on the thermal equilibrium assumption, only one energy equation is solved

$$\rho_{eff}c_{p,eff}\nabla \bullet (\mathbf{V}T) = \nabla \bullet \left(k_{eff}\nabla T - \sum_{i=1}^{n} \dot{\mathbf{m}}_i h_i\right) + S_T \tag{7}$$

Eq. (7) balances the convected energy, the heat conduction through the solid and the gas mixture, the energy due to fuel gas species diffusion, and a source term S_T. It should be mentioned that the gas species diffusion related thermal energy is accounted for in both the gas flow duct and the active reaction region. In Eq. (7) h_i is the partial enthalpy of the ith species and is obtained from [10]

$$h_i = h_{form,i} + \int_{T_0}^{T} c_{pi}(T)\,dT \tag{8}$$

where $h_{form,i}$ is the specific enthalpy of formation of the ith gas species at $T = T_0 = 298.15$ K. The heat source term S_T in Eq. (7) is associated with the steam reforming, water gas-shift and reverse methanation reactions,

$$S_{\mathrm{T}} = \sum_i R_i \Delta h_{\mathrm{reaction},i} \tag{9}$$

where R_i is the reaction rate, and $\Delta h_{\mathrm{reaction},i}$ is the reaction enthalpy.

The species mass conservation equations are written in the general form,

$$\nabla \bullet (\rho_{\mathrm{eff}} \mathbf{V} Y_i) = \nabla \dot{\mathbf{m}}_i + S_{\mathrm{s},i} \tag{10}$$

where Y_i is the mass fraction of the ith fuel gas species, $\dot{\mathbf{m}}_i$ represents the mass diffusive flux of species, and $S_{\mathrm{s},i}$ the production/consumption rate of the ith fuel species. The above equation is solved for H_2, CH_4, CO and H_2O, respectively, i.e., for $n-1$ species where n is the total number of species involved in the fuel gas mixture. The mass fraction of the nth species (CO_2) can be obtained from the requirement that the sum of the mass fractions equals one.

Mass diffusion is a process leading to equalization of substance fraction or establishing an equilibrium gas distribution that results from random migration of the species. Molecular diffusion occurs as a result of thermal motion of the molecules, and the flux of the species i is proportional to the fraction gradient and diffusion coefficient. One of the significant challenges in fuel reforming modelling is in determining the rate at which the species diffuse and gases convect in the fuel flow ducts and porous catalytic areas. This requires knowledge of multi-component diffusion in the fuel flow ducts, particularly in the porous catalytic layers. In the literature, there are several basic approaches for determining the molar diffusion flux $\dot{\mathbf{n}}_i$ and converting to mass diffusion flux $\dot{\mathbf{m}}_i$ via the species molar mass, i.e., $\dot{\mathbf{n}}_i = \dot{\mathbf{m}}_i / M_i$. Fick's law, represented by $\dot{\mathbf{n}}_i = -\rho D_{i,j} \nabla X_i$ based on binary diffusion coefficient $D_{i,j}$ and molar fraction X_i, is the simplest diffusion model and is typically used in binary or dilute system [11]. A multi-component mixture extension of Fick's law is sometimes used in the literature as well, e.g., in [13], and also applied in this study,

$$\dot{\mathbf{n}}_i = -\rho D_{i,\mathrm{gm}} \nabla X_i + X_i \sum_{i=1}^{n} \dot{\mathbf{n}}_j \tag{11}$$

The diffusion coefficients of species i in the gas mixture for the fuel gas flow duct are calculated by the expression based on the binary coefficients [11]

$$D_{A,\mathrm{gm}} = \frac{1 - X_A}{X_B/D_{AB} + X_C/D_{AC} + \cdots} \tag{12}$$

where $D_{A,\mathrm{gm}}$ is the diffusion coefficient of the component A in the mixture with $B, C, \ldots, X_A, X_B, X_C$ are the molar fraction of the appropriate species, and D_{AB} and D_{AC} are the diffusion coefficients in the AB and AC binary system, respectively. It is clear that for an n component system, $n(n-1)/2$ binary diffusivities are required.

For the porous catalytic reaction area, molecular diffusion is predominant in the case with large pores, whose size is much bigger than the mean free-path of the diffusion gas molecules. In this case, diffusion can be described as presented above for the fuel flow duct. Knudsen diffusion occurs in porous layer with small pores or under low pressure when the mean free-path of molecules is larger than the pore size, and the molecules collide with the walls more often than between themselves. In order to calculate the Knudsen diffusion flux, the coefficient $D_{i,\mathrm{k}}$ is calculated based on the free molecule flow theory [11]

$$D_{i,\mathrm{k}} = \frac{2}{3} r_{\mathrm{e}} v_i = \frac{2}{3} r_{\mathrm{e}} \left(\frac{8 \Re T}{\pi M_i} \right) \tag{13}$$

in which r_{e} is the effective radius and v_i the average molecular speed of the ith gas species. To account for the reduction in the cross-sectional area and the increased diffusion length due to the tortuous paths of real pores in the porous catalytic layer, the effective diffusion coefficient can be evaluated [5,11]

$$D_{i,\mathrm{eff}} = \frac{\varepsilon}{\tau} \left(\frac{D_{i,\mathrm{gm}} \times D_{i,\mathrm{k}}}{D_{i,\mathrm{gm}} + D_{i,\mathrm{k}}} \right) \tag{14}$$

where ε is the porous porosity, and τ the tortuosity. The most common reforming reactor is based on Ni by alumina support, with the Ni content 7–15% [5].

There exist various reaction kinetics and rate/equilibrium constants reported in the literature for the reactions. A general rate equation based on Langmuir–Hinselwood–Hougen–Watson (LHHW) approach [5,12] describes most accurately the process for a wide range of parameters, and is applied in this study to express the kinetic rates of absorption or production of the gas species, based on partial pressure, temperature and species compositions for the chemical reactions (1)–(3)

$$R_1 = \frac{\frac{k_1}{p_{\mathrm{H_2}}^{2.5}} \left(p_{\mathrm{CH_4}} p_{\mathrm{H_2O}} - \frac{p_{\mathrm{H_2}}^3 p_{\mathrm{CO}}}{K_{e,1}} \right)}{(\mathrm{Den})^2} m_{\mathrm{cl}}, \quad \mathrm{kmol/(m^3\,s)} \tag{15}$$

$$R_2 = \frac{\frac{k_2}{p_{\mathrm{H_2}}} \left(p_{\mathrm{CO}} p_{\mathrm{H_2O}} - \frac{p_{\mathrm{H_2}} p_{\mathrm{CO_2}}}{K_{e,2}} \right)}{(\mathrm{Den})^2} m_{\mathrm{cl}}, \quad \mathrm{kmol/(m^3\,s)} \tag{16}$$

$$R_3 = \frac{\frac{k_3}{p_{\mathrm{H_2}}^{3.5}} \left(p_{\mathrm{CH_4}} p_{\mathrm{H_2O}}^2 - \frac{p_{\mathrm{H_2}}^4 p_{\mathrm{CO_2}}}{K_{e,3}} \right)}{(\mathrm{Den})^2} m_{\mathrm{cl}}, \quad \mathrm{kmol/(m^3\,s)} \tag{17}$$

in which, m_{cl} is the catalyst loading ($\mathrm{kg_{cat}/m^3}$), and $\mathrm{Den} = 1 + K_{\mathrm{CO}} p_{\mathrm{CO}} + K_{\mathrm{H_2}} p_{\mathrm{H_2}} + K_{\mathrm{CH_4}} p_{\mathrm{CH_4}} + K_{\mathrm{H_2O}} p_{\mathrm{H_2O}} / p_{\mathrm{H_2}}$. The values of the pre-exponential factors, activation energies,

Table 2
Kinetic parameters and equilibrium constants [5]

Reaction	Kinetic rate constant k_i (kmol/$\mathrm{kg_{cat}}$ h)	Equilibrium constant K_{ej}
Steam reforming	$4.225 \times 10^{15} \times \mathrm{e}^{(-240100/RT)}$	$5.75 \times 10^{12} \times \mathrm{e}^{(-11476/RT)}$, $\mathrm{bar^2}$
Water gas-shift	$1.955 \times 10^{6} \times \mathrm{e}^{(-67130/RT)}$	$1.26 \times 10^{-2} \times \mathrm{e}^{(4639/RT)}$
Reverse methanation	$1.02 \times 10^{15} \times \mathrm{e}^{(-243900/RT)}$	$7.24 \times 10^{10} \times \mathrm{e}^{(-21646/RT)}$, $\mathrm{bar^2}$

Table 3
Adsorption constants K_i [5]

Species	CH_4	CO	H_2	H_2O
K_i	$6.65\times10^{-4}\times e^{(-38280/RT)}$, bar^{-1}	$8.23\times10^{-5}\times e^{(-70650/RT)}$, bar^{-1}	$6.12\times10^{-9}\times e^{(-82900/RT)}$, bar^{-1}	$1.77\times10^{5}\times e^{(88680/RT)}$, –

equilibrium constants, and heat of adsorption are given in Tables 2 and 3, respectively.

In Eq. (10), the source terms $S_{s,i}$ read

$$\begin{aligned} S_{s,H_2} &= (3R_1 + R_2 + 4R_3)M_{H_2};\\ S_{s,CH_4} &= (-R_1 - R_3)M_{CH_4};\\ S_{s,H_2O} &= (-R_1 - R_2 - 2R_3)M_{H_2O};\\ S_{s,CO} &= (R_r - R_s)M_{CO} \end{aligned} \tag{18}$$

The effective thermal conductivity k_{eff} and effective specific heat are estimated by considering the porous catalytic layer effects, i.e.,

$$k_{eff} = \varepsilon k_f + (1-\varepsilon)k_s \tag{19}$$

$$c_{p,eff} = \varepsilon c_{p,f} + (1-\varepsilon)c_{p,s} \tag{20}$$

Based on the reforming reaction function, the thermal and fuel gas mass fraction/flux boundary conditions at the walls are as follows. It should be noted that the heat input to the steam reforming duct is from the catalytic combustion zone which is not included in this study, and the supplied heat is then considered as a constant value of the heat flux q_b at the bottom wall, see the lower diagram of Fig. 1.

At the bottom wall ($y = 0$):

$$U = V = W = 0; \quad q_b = -k_{eff}\frac{\partial T}{\partial y}; \quad J_i = -\rho_{eff}D_{i,eff}\frac{\partial Y_i}{\partial y} = 0 \quad (i = H_2, CO, H_2O \text{ and } CH_4) \tag{21}$$

at the top and side walls:

$$U = V = W = 0, \quad q = 0, \quad J_i = 0 \tag{22}$$

at the mid-plane ($z = a/2$):

$$\frac{\partial U}{\partial z} = \frac{\partial V}{\partial z} = W = \frac{\partial T}{\partial z} = \frac{\partial Y_i}{\partial z} = 0 \tag{23}$$

In the present investigation, the interfacial boundary conditions, commonly employed in the literature, are applied for the continuity of shear stress, heat and mass flux:

$$(\mu_{eff}\partial U/\partial y)_- = (\mu_f \partial U/\partial y)_+ \tag{24}$$

$$(k_{eff}\partial T/\partial y)_- = (k_f \partial T/\partial y)_+ \tag{25}$$

$$(\rho_{eff}D_{i,eff}\partial Y_i/\partial y)_- = (\rho_f D_{i,gm}\partial Y_i/\partial y)_+ \tag{26}$$

Here subscript + (plus) stands for fuel flow duct side, − (minus) for porous catalytic layer side. Moreover, the thermal interfacial condition, Eq. (25), is also applied at an interface between the porous catalytic layer and the solid plate with k_s instead of k_f.

It is clear that the approach applied in this study is based on one set of governing equations with the extra source terms and the transport properties' modification, which enables the porous reaction and pure fluid flow regions to be treated as a single domain. This approach has been successfully used in the fuel cell and reformer modelling society, particularly for cases involving the composite domains as in this study.

If the detailed analysis is required for the transport phenomena and chemical reactions in the pure porous region, the multi-component Stefan–Maxwell mass diffusion equation should be applied to cover the continuum, slip, free molecular and transition regions based on the porous structure and operating conditions. For this case, the optimal porous structure design and catalyst loading/distribution could be the major targets of the analysis.

4. Numerical solution methodology

A three-dimensional CFD code was applied to solve the governing Eqs. (3), (4), (6) and (8), together with the boundary conditions (21)–(23) and interfacial conditions (24)–(26). The code is a general purpose one and is based on the finite-volume technique with boundary fitted coordinates for solving the differential equations. The Cartesian coordinate system in the physical space is replaced by a general non-orthogonal coordinate system. The momentum equations are solved for the velocity components on a non-staggered grid arrangement. The Rhie–Chow [14] interpolation method is used to compute the velocity components at the control volume faces. Algorithms based on the TDMA (Tri-Diagonal Matrix Algorithm) and a modified SIP (Strongly Implicit Procedure) are employed for solving the algebraic equations. In this study, the convective terms are treated by the QUICK (Quadratic Upstream Interpolation Convective Kinematics) scheme, while the diffusive terms are treated by the central difference scheme. The SIMPLEC (Semi-Implicit Method for Pressure-Linked Equations-Consistent) algorithm handles the linkage between velocities and pressure.

As shown above, the equations needed for the calculation are coupled by temperature, partial pressure/fraction of gas species via source terms and thermal-physical properties. It is clear that no gas flow is present in the solid plates. Eqs. (3), (5) and (8) are then blocked out and only the heat conduction equation, derived from the energy equation (6), is solved for this domain. As mentioned earlier, the thermal-physical properties of the gas mixture are variable. These parameters depend on the position in the duct, and the species mass fraction and/or temperature as well. Fuel gas mixture density, viscosity and specific heat are then calculated and updated during the calculations.

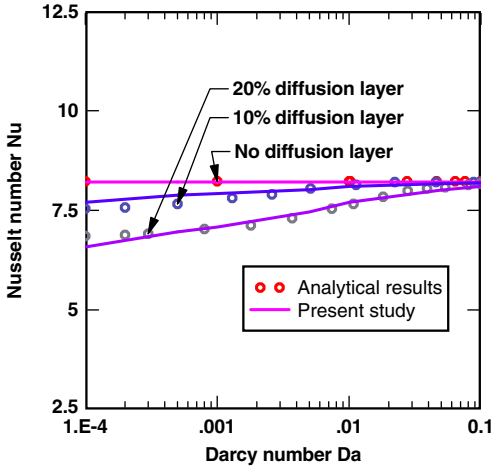

Fig. 2. Fully developed Nusselt number Nu variation in a parallel plate duct vs. Darcy number ($Da = \beta/h^2$), compared with the analytical ones from [15].

A uniform grid point distribution over the cross section is used. To obtain finer meshes in the entrance region of the duct, a non-uniform distribution of grid points with an expansion factor is implemented for the main flow direction. Various values of the expansion factor have been checked and 1.01 was found to be sufficient to achieve grid independent solutions.

In order to evaluate the performance of the numerical method and code, test calculations considering grid sensitivity, code performance and validation were carried out. It has been found that the predictions do not change significantly in terms of fuel species distributions, when the number of grid points is increased beyond $70 \times 70 \times 50$ (70×50 for the cross section, 70 for the main flow direction). Calculations have been carried out for fully developed conditions in a parallel plate duct for various thicknesses of the porous layer and the same boundary conditions of constant heat flux on the walls. The comparison in Fig. 2 shows that the computed values of Nusselt numbers Nu agree well with the analytical ones in [15].

5. Results and discussion

Configuration and operating parameters of a typical reforming duct are applied as a base case in this study. To investigate the effects on the transport phenomena and performance, parameter studies are conducted by changing one of the base case parameters. Table 4 shows the base geometry parameters. For the porous layer, the parameters are chosen as: porosity $\varepsilon = 0.5$, permeability $\beta = 2 \times 10^{-10}$ m^2, and catalyst loading $m_{cl} = 1$ g$_{cat}$/cm^3. The binary diffusion coefficients of the fuel species are shown in Table 5 [16]. Fuel inlet temperature $T_{in} = 650$ °C; inlet mole fraction H_2:CH_4:CO:H_2O:CO_2 = 0.026:0.2470:0:0.7145:0.0125 with $U_{in} = 5$ m/s. It should be noted that all the results presented hereafter are for the base case condition unless otherwise stated.

Table 4
Geometries of the reforming reaction duct (cm)

	Length $L(x)$	Depth $h(y)$	Width a or $b(z)$
Overall duct	20	1	0.5
Fuel flow duct	20	0.4	0.4
Porous catalytic layer	20	0.4	0.5

Table 5
Binary diffusivity of the ith fuel gas species

i/j	$D_{i,j}$ (m^2/s)	i/j	$D_{i,j}$ (m^2/s)
CH_4/CO	3.47e−05	CO/H_2	11.92e−05
CH_4/H_2O	4.30e−05	CO/CO_2	2.59e−05
CH_4/H_2	11.04e−05	H_2O/H_2	14.10e−05
CH_4/CO_2	2.88e−05	H_2O/CO_2	3.38e−05
CO/H_2O	4.15e−05	H_2/CO_2	10.23e−05

5.1. Analysis of transport processes for the base case condition

The main results of the numerical simulations are reported and discussed in this section. Fig. 3a shows the velocity contours profile along the main flow direction. Due to the permeation and mass generation/consumption effects by the reforming reactions, the uniform distribution and the symmetry of the axial velocity associated with a pure forced duct flow do not exist any more, and the position of the maximum values shifts away from the central plane ($y/h = 0.7$ in Fig. 3a). On the other hand, the velocity in the porous catalyst layer is very small except in the region close to the fuel gas duct, because the gas penetration into the porous layer is weak. A small convective gas flow is then identified only in the porous catalytic layer close to the fuel flow duct.

The steam reforming reaction can be found in Fig. 3b, represented by the hydrogen mole distribution in the duct particularly in the porous catalyst layer. The porous catalyst layer is occupied by higher H_2 fraction than that in the fuel flow duct resulting from the steam reforming reaction (Eq. (1)), shift reaction (Eq. (2)) and reverse methanation reaction (Eq. (3)), as shown in Fig. 3b. A large amount of H_2 is produced in the interface region of the porous catalytic layer close to the fuel duct, which is reflected by a sharp increase of H_2 mole fraction. As revealed later in this paper, this region is confined mainly up to around 10% of the overall duct height (i.e., 1 mm) into the porous catalyst layer at most of the stations along the main flow direction, except at the inlet area where the reactions take place more deeply into the porous layer.

Hydrogen mole fraction profiles are plotted in Fig. 4 for the cross section at various stations. It is found that, in a cross section, the H_2 mole fraction has maximum values close to the bottom solid plate, which is caused by the reforming reaction mentioned above. Almost uniformly distributed mole fraction can be found in both the fuel flow duct and the porous catalyst layer. However, a bigger

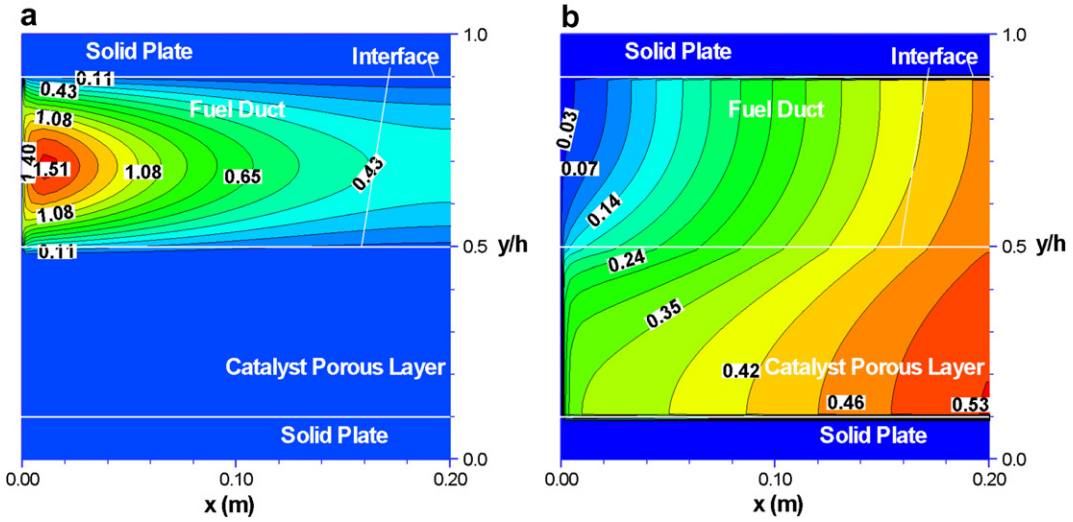

Fig. 3. (a) Velocity contours and (b) H_2 mass fraction distribution along main flow direction of the fuel reforming duct.

value has been predicted in the porous layer close to the side wall.

CO, CH_4 and CO_2 mole fraction profiles along the main flow direction are shown in Fig. 5. It is found that the CO fraction increases monotonically along the depth of the porous catalyst layer close to interface areas. This is due to the net generation of CO during the steam reforming reaction (CO generation) and the water gas-shift reaction

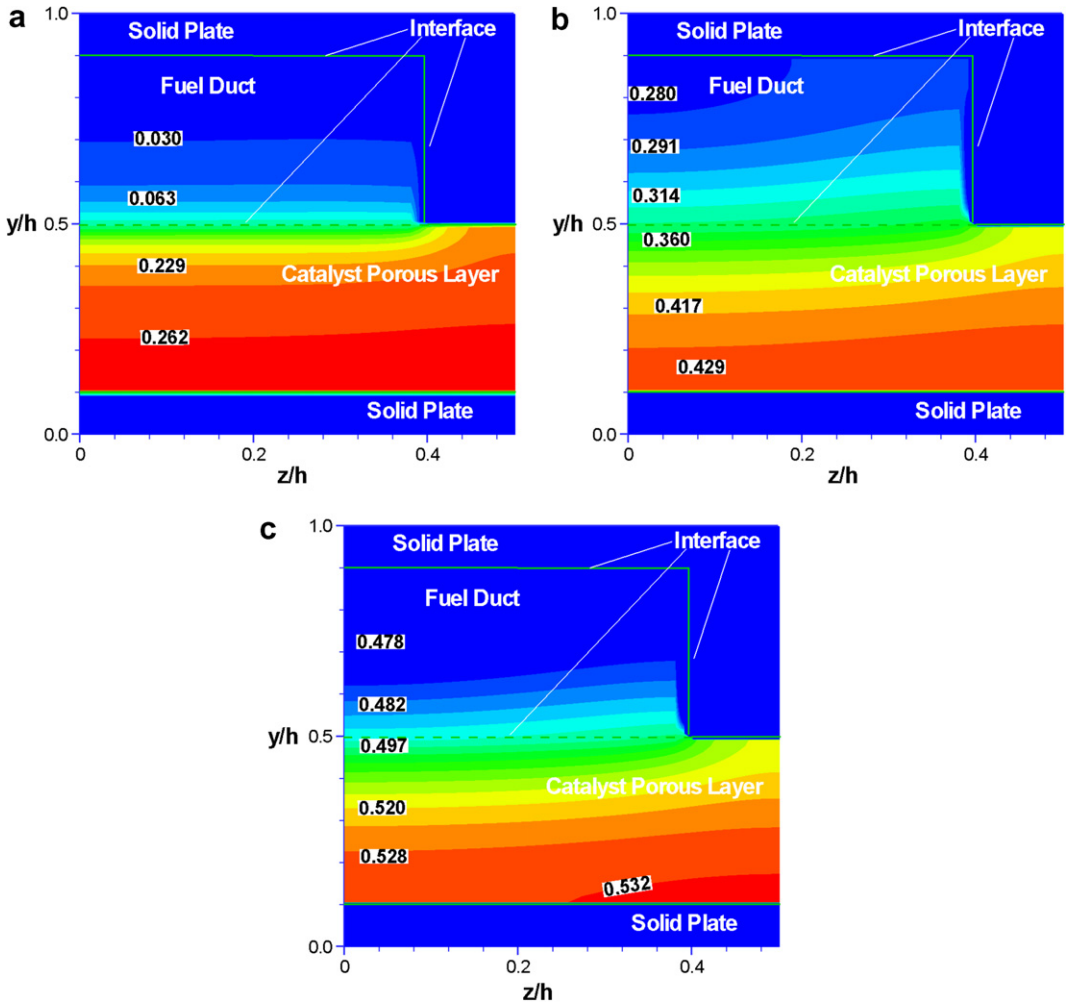

Fig. 4. Cross-sectional H_2 mole fraction distributions at: (a) the inlet; (b) 1/2 length from the inlet; and (c) the exit of a steam reforming reaction duct.

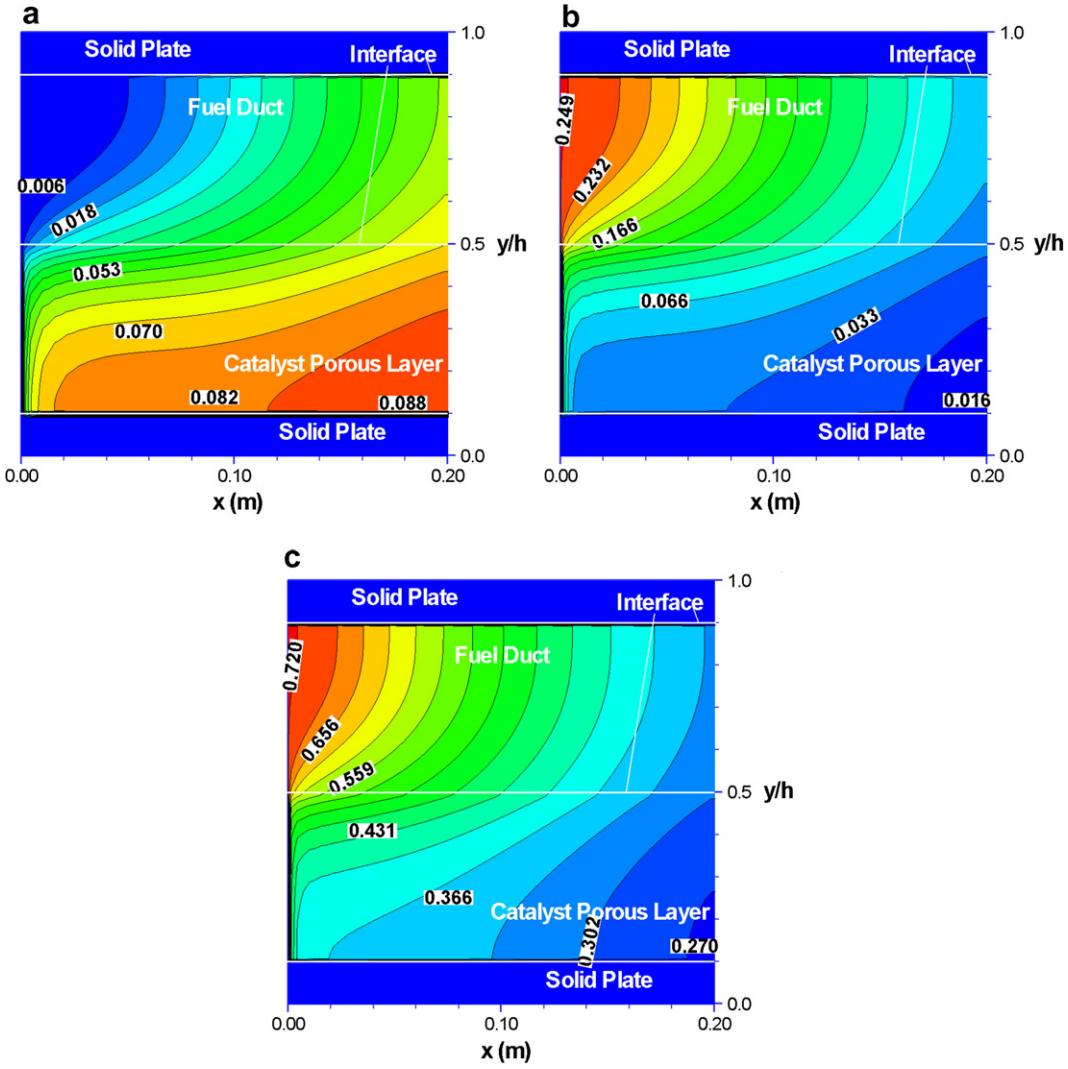

Fig. 5. (a) CO; (b) CH_4; and (c) H_2O mole fraction distributions along main flow direction of a steam reforming reaction duct.

(CO consumption). As revealed later, the first reaction is much faster than the latter one. Moreover, the gradient of the CO fraction in the direction normal to the active wall (the bottom solid plate in Fig. 1) is larger close to interface area if compared to other regions. On the other hand, a large amount of CH_4 is reacted in the interface region of the porous layer close to the fuel duct, which is reflected by a sharp decrease of CH_4 mole fraction, as shown in Fig. 5b. Water activities in the duct are shown in Fig. 5c. It is observed that H_2O is consumed in the porous catalyst regions by all the reactions mentioned above. For this reason, the mole fraction of H_2O decreases along the main flow direction and towards the interface of the solid wall/porous catalyst layer.

The reaction rates for the steam reforming, the water gas-shift and reverse methanation reactions are shown in Fig. 6a–c, respectively. All the reactions appearing in Eqs. (1) and (3) are strong in the interface region of the porous catalyst layer close to the fuel duct (with big reaction rate values), and weak in the rest of the porous layers. However, for the water gas-shift reaction in Eq. (2), the reaction rate is small compared to the other reactions in all the reaction regions, as shown in Fig. 6b. The maximum reaction rates are 0.170, 0.0001 and 2.146 kmol/(m^3 s) for the steam reforming, water gas-shift and reverse methanation reactions, respectively, at the base condition.

It is clear that the temperature increases steadily along the main flow direction in Fig. 7. The variation in temperature distribution can also be observed in the vertical direction with a larger value at the bottom solid plate. These are created by the heat flux supplied by the catalytic combustion (modelled by a constant heat flux $q_b = 1000$ J/(m^2 s) in this study).

5.2. Effects of the operating temperature

Fig. 8 shows the CH_4 mole fraction profiles for various operating temperatures. By comparing with Fig. 5b, it is found that the CH_4 mass fraction decreases slowly in both

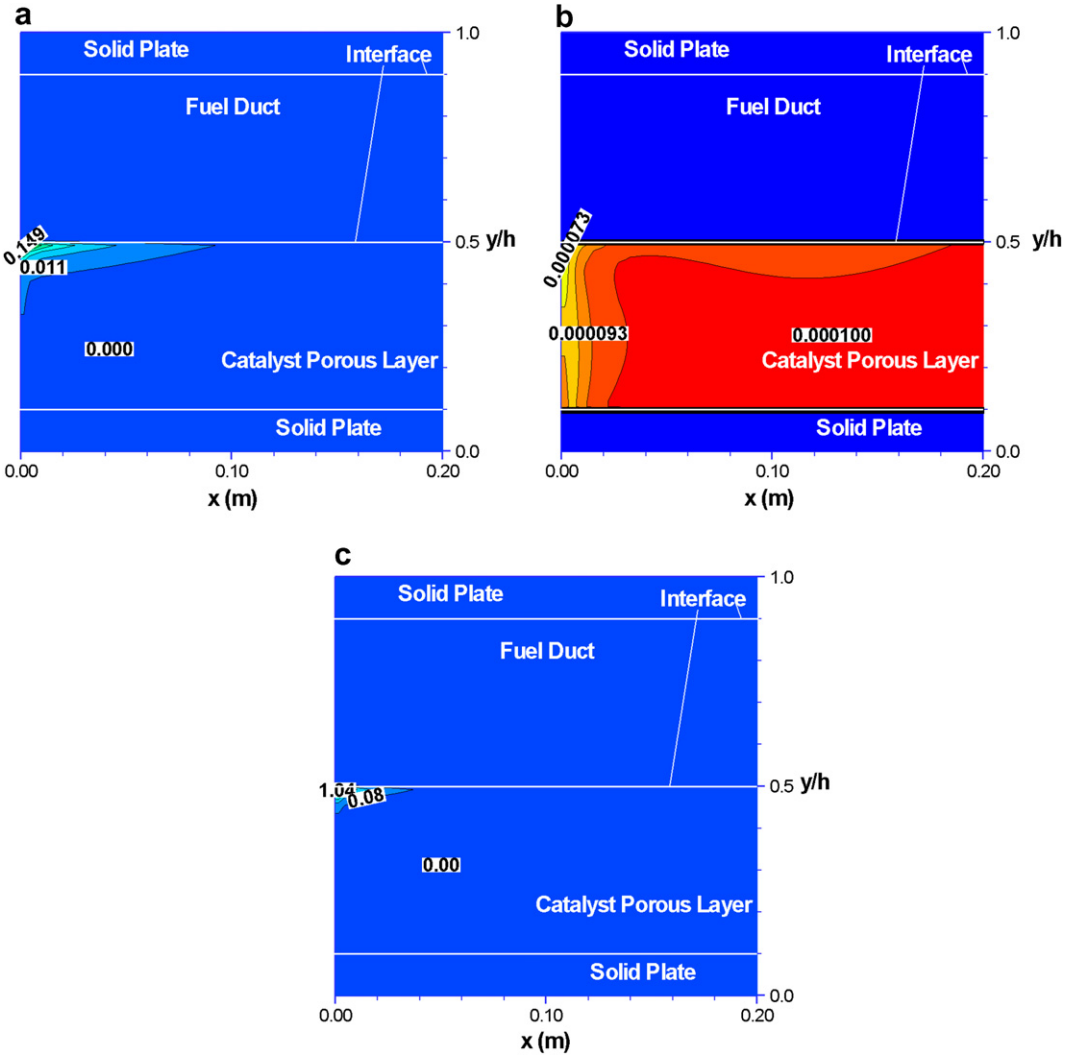

Fig. 6. Distribution of: (a) steam reforming reaction; (b) water gas-shift reaction; and (c) reverse methanation reaction rates along main flow direction of a reaction duct.

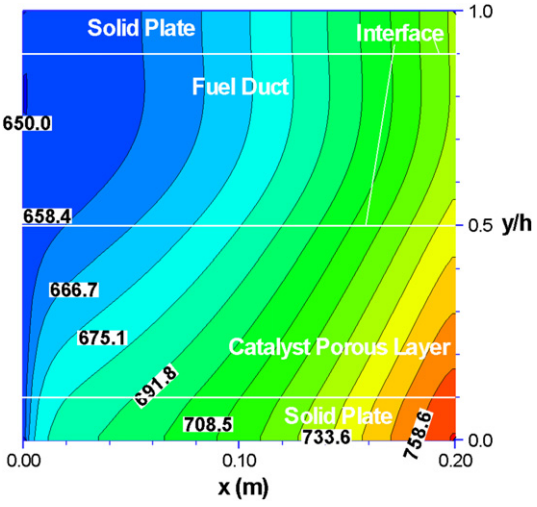

Fig. 7. Temperature contour profile along main flow stream of a reaction duct at the base condition.

the main flow stream and the vertical direction at a lower temperature, i.e., 600 °C in Fig. 8a, compared to 700 °C in Fig. 8b. It is so because the reforming reactions depend on the temperature, i.e., higher temperature causes faster reactions (bigger values of the maximum reaction rates). For this specific design, the methane mole conversion efficiency at the exit of the fuel duct reaches 95% at higher operating temperature (700 °C), as shown in Table 6.

5.3. Effects of the catalyst loading

The CH_4 mole fraction profiles for various catalyst loadings are presented in Fig. 9. It is clear that large catalyst loading (10 vs. 1 g_{cat}/cm^3) yields a big CH_4 conversion, as shown in Fig. 9b and Table 6. The most common industrial catalyst is based on Ni on alumina support, with Ni content 7–15% [5]. An important aspect of catalyst design and performance analysis concerns net catalyst loading or/and effective surface area. It is preferable to use a

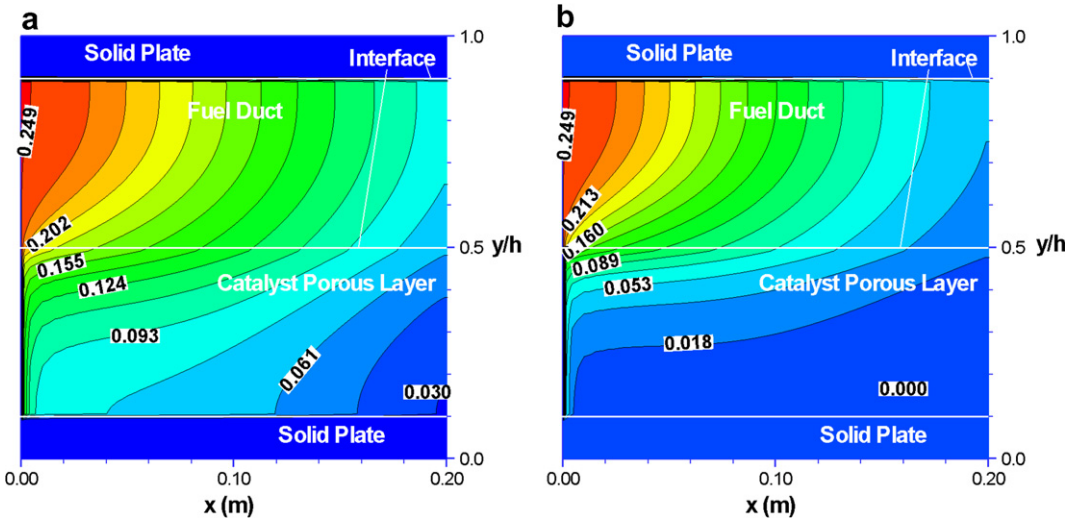

Fig. 8. CH_4 mass fraction distributions along the main flow direction of a steam reforming reaction duct at: (a) 600 °C and (b) 700 °C at the base condition.

parameter like the specific surface area, i.e., the active surface area per unit volume of porous catalyst structure. The reaction rates can be stated per unit area of catalyst surface, which is independent of the particular support structure and catalyst loading. Due to the lack of available data for the specific surface area, however, the net catalyst loading is specified as a relevant parameter for the analysis in this study.

Table 6
The predicted reactor performance at various temperatures and catalyst loadings

Catalyst loading, g_{cat}/cm^3	Temperature, °C	Steam reforming reaction rate $R_{r,max}$, kmol/(m^3 s)	Water gas-shift reaction rate $R_{s,max}$, kmol/(m^3 s)	Reverse methanation reaction rate $R_{re,max}$, kmol/(m^3 s)	Methane conversion, %
1	600	0.065	0.00008	0.618	71.60
	650	0.170	0.0001	1.198	81.68
	700	0.398	0.0002	2.146	88.44
10	600	0.224	0.0006	1.403	85.06
	650	0.580	0.0010	2.699	91.03
	700	1.393	0.0017	5.070	94.55

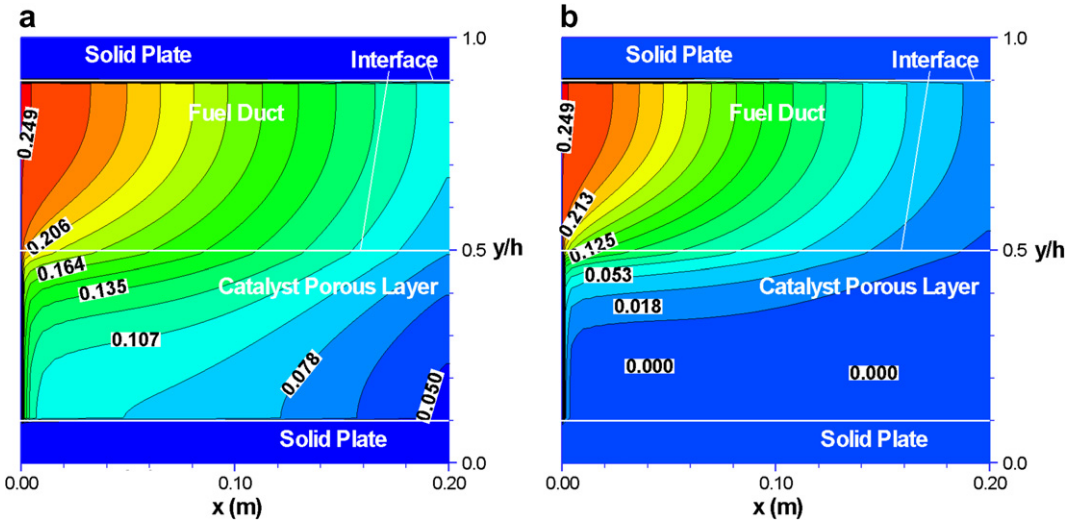

Fig. 9. CH_4 mole fraction distributions along the main flow direction of a steam reforming reaction duct with the catalyst loading of: (a) 0.1 and (b) 10 g_{cat}/cm^3.

It should be noted that the methane conversion efficiency is defined in the conventional manner, i.e., the ratio of mole CH_4 fraction at the reformer exit and the one at the inlet $(X_{CH_4,exit}/X_{CH_4,inlet})$. From Table 6, it is found that the maximum reaction rates increase when the catalyst loading is big, and the same does the methane conversion efficiency. For certain catalyst loading, increasing in temperature has an effect to promote all reactions (big maximum reaction rates) and the methane conversion efficiency.

5.4. Effects of the porous catalytic reaction layer

The effects of the porous catalytic reaction layer on the fuel gas flow are shown and discussed in the following section. It is noted from Fig. 10a that, by decreasing the permeability, fuel gas permeation to the porous layer is small, i.e., the axial velocity is zero for the most regions of the porous layer. This is so because the permeability is a term used for the conductivity of the porous medium with respect to permeation by a fluid. It is known that a small permeability of a porous layer allows less gas to pass at the same pressure gradient. As for a big permeability in Fig. 10b, more fuel gas is permeated from the flow duct, and as a result the gas convection can be found with bigger velocities in the porous layer close to the fuel flow duct at the entrance region. Consequently, certain impacts on the change of the axial velocity distribution are expected for both the flow duct and the porous catalytic layer, when the permeability is higher.

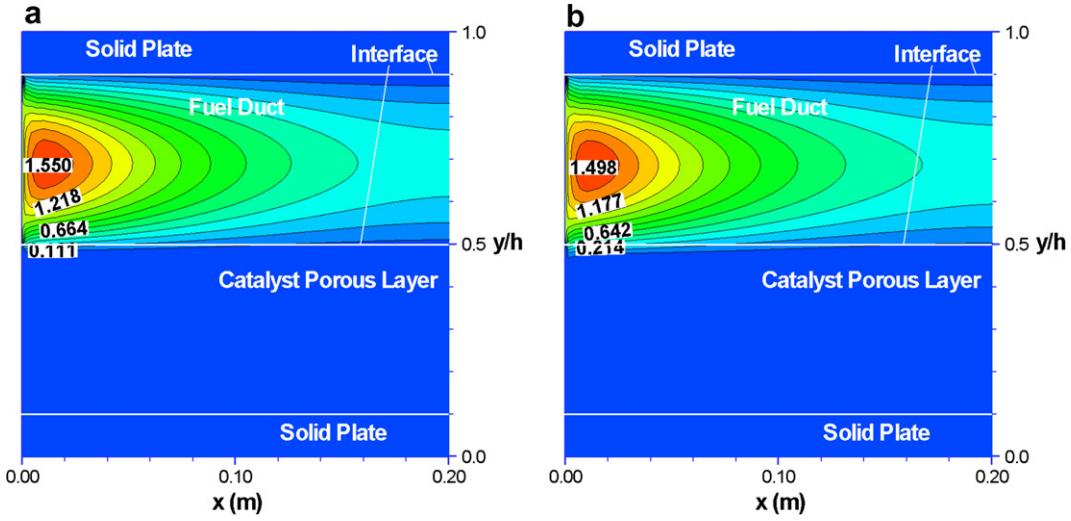

Fig. 10. Dimensionless axial velocity contours at permeability of: (a) $\beta = 5.0 \times 10^{-11}$ m^2 and (b) $\beta = 5.0 \times 10^{-9}$ m^2 along the main flow direction of a steam reforming reaction duct at the base condition.

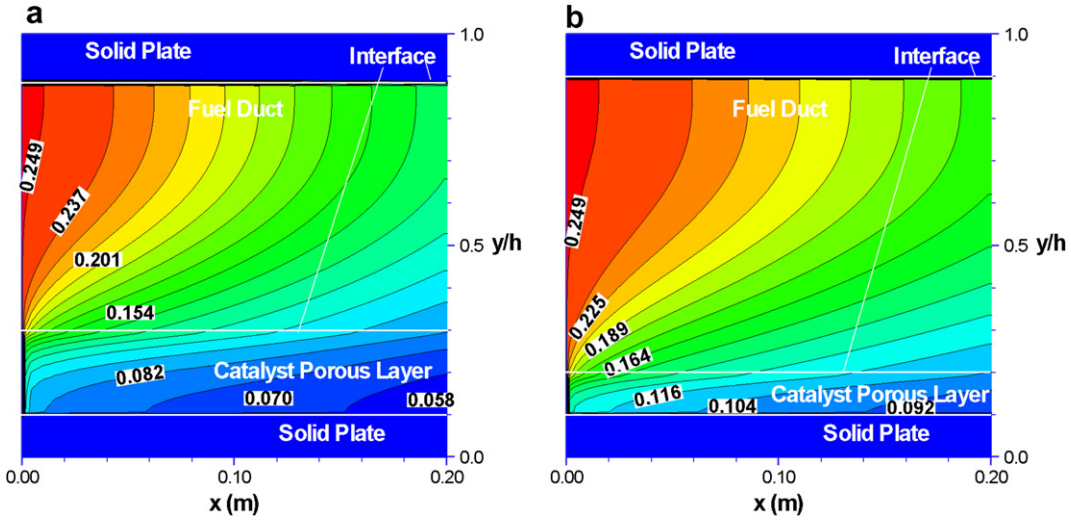

Fig. 11. Effects of the thickness of the porous reforming layer on CH_4 mole fraction distributions along the main flow direction of a steam reforming reaction duct: (a) the porous layer thickness $h_p = 2$ mm and (b) $h_p = 1$ mm.

As expected, thickness of the porous catalytic layer is one of the most important parameters. The effects on the transport processes and reforming reactions have also been investigated in this paper. To investigate effects of the porous layer thickness on the gas flow and reformer performance, the height of porous layer h_p and gas flow duct h_d were varied while other parameters were kept constant. Compared to Fig. 5b, it is noted that the thinner porous layers (thickness $h_p = 2$ and 1 mm, respectively, vs. 4 mm) predict bigger mole CH_4 mole fraction, and then smaller CH_4 conversions efficiency are obtained. The methane conversion efficiencies at the reformer exit are 56.66% and 44.87% for the cases in Fig. 11a and b, respectively, compared to 81.68% for the base condition. However, bigger steam reforming reaction rates (with big values, not small ones) in Eq. (1) are observed for thin reaction layers, as shown in Fig. 12a and b. This is due to higher CH_4 mole fraction in the porous catalytic layer, because the CH_4 mole fraction has positive effects to promote fast reactions of steam reforming in Eq. (1) and reverse methanation in Eq. (3) (not shown in this study).

Fig. 13 shows the temperature distributions to reveal the porous layer thickness effects. It is found that the thinner porous layers have small temperatures in both the fuel flow duct and the porous catalytic layers. For instance, the maximum temperatures appearing in the active plate corner (the bottom plate in Fig. 1) at the exit are 712 °C and 694 °C for the cases in Fig. 13a and b, respectively, compared to 758.6 °C for the base condition (see Fig. 7). It is so because the steam reforming reaction rates in Eq. (1)

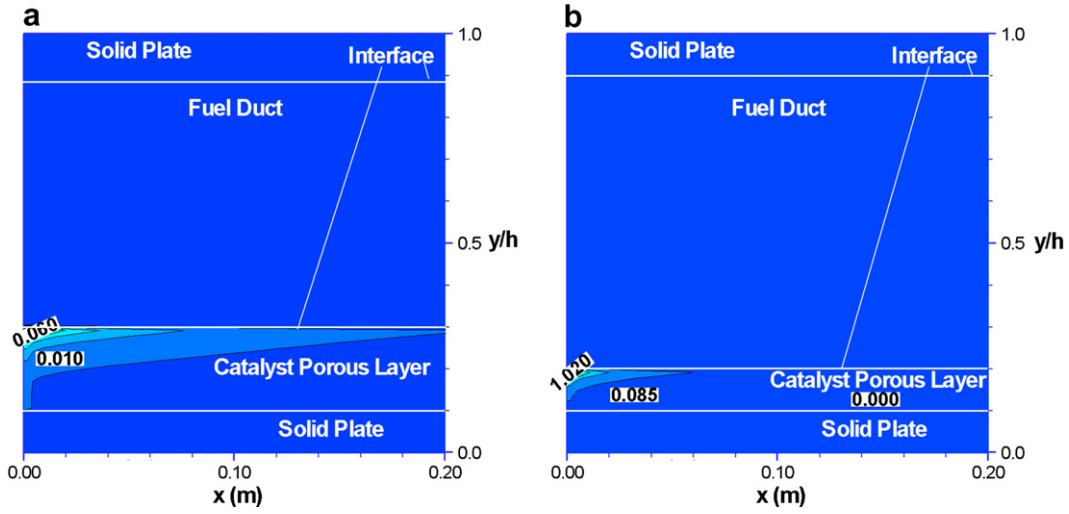

Fig. 12. Effects of the thickness of the porous reforming layer on distribution of steam reforming reaction rate along main flow direction of a reformer duct: (a) porous layer thickness $h_p = 2$ mm and (b) 1 mm.

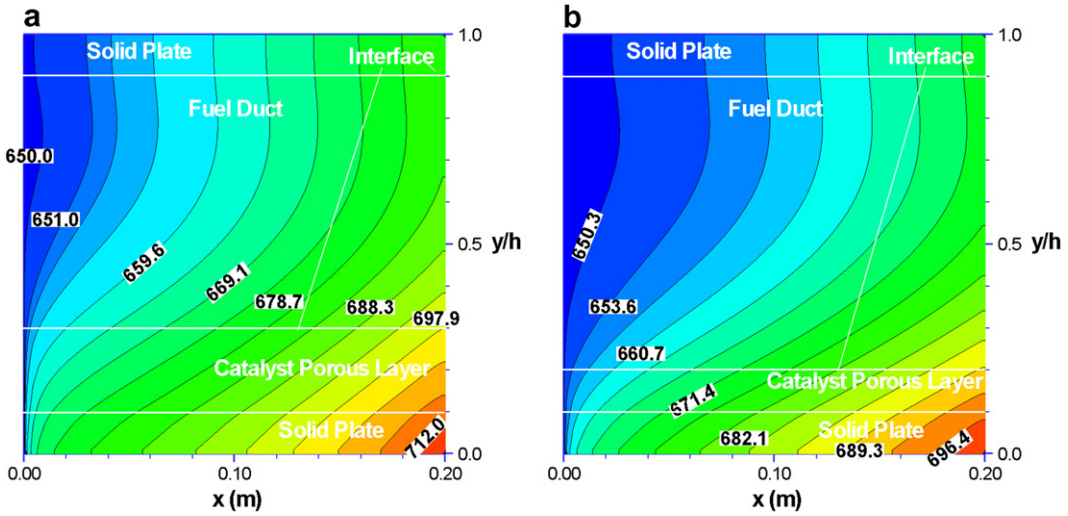

Fig. 13. Effects of the porous catalytic layer thickness on temperature distribution along main flow direction of a reformer duct: (a) porous layer thickness $h_p = 2$ mm and (b) 1 mm.

are bigger and more heat is consumed, when the thinner porous catalytic layers are employed.

As revealed in [9], three characteristic ratios have significant effects on various transport processes in composite ducts (gas flow duct and porous layer). These are the hydraulic diameter ratio D_{hr} (ratio of the porous layer diameter to the gas flow duct diameter), the permeation length ratio PL_r (ratio of the porous layer width to the gas flow duct width), and the permeation rate ratio PR_r (ratio of the entrance pressure gradient to permeation resistance).

$$D_{hr} = D_{hp}/D_{hd} \tag{27}$$

$$PL_r = a/b \tag{28}$$

$$PR_r = (\rho U_{in}^2/2h_p)/(\mu U_{in}/\beta) = (\rho\beta U_{in})/(2\mu h_p) \tag{29}$$

D_{hp} in Eq. (27) is the hydraulic diameter of the porous catalytic layer, D_{hd} the hydraulic diameter of the gas flow duct; a in Eq. (28) is the width of porous layer, b the width of the flow duct; h_p in Eq. (29) is the thickness of the porous layer. It is clear that both diameter ratio D_{hr} and permeation length ratio PL_r are related to the gas flow duct and porous catalytic layer configurations, to account for the characteristics of the permeation area and length, respectively. The permeation rate ratio PR_r considers the characteristics of the porous catalytic material (such as the permeability β_i) and duct operation parameter (such as the inlet velocity U_{in}). It is clear that the thickness of the porous catalytic layer has opposite roles in the diameter ratio and permeation rate ratio, i.e., a thinner porous layer generates a smaller diameter ratio D_{hr}, however a bigger permeation rate ratio. As a result, the thickness of the por-

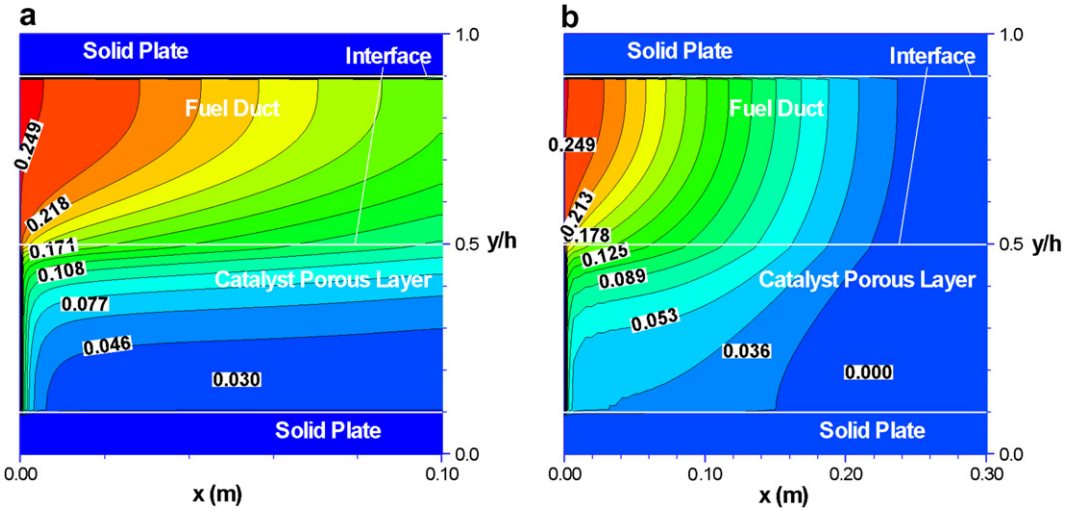

Fig. 14. The reformer length effects on CH_4 mole fraction distributions along the main flow direction at: (a) $L = 10$ cm and (b) $L = 30$ cm at the base condition.

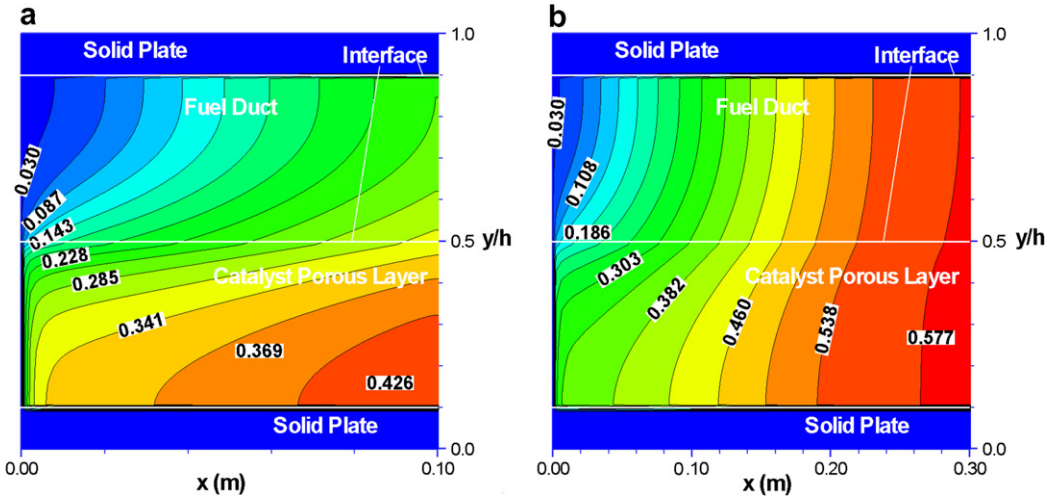

Fig. 15. The reformer length effects on H_2 mole fraction distributions along the main flow direction at: (a) $L = 10$ cm and (b) $L = 30$ cm at the base condition.

ous layer has composite effects on the transport processes and reformer performance. Further study is needed to find an optimal thickness of the porous catalytic layer.

5.5. Effects of the reformer length

The reformer length effects on the CH_4 mole fraction profiles are presented in Fig. 14. It is found that shorter reformer ($L = 10$ cm) predicts big CH_4 mole fractions, as shown in Fig. 14a. While for a longer reformer ($L = 30$ cm), all the supplied CH_4 has been reformed, and the mole fractions are zero in both the porous catalytic layer and the gas flow duct close to the exit. The methane conversion efficiencies yield 48.78% ($L = 10$ cm) and 99.60% (for $L = 30$ cm), respectively, compared to 81.68% at the base condition (for $L = 20$ cm) in Fig. 5b. The similar trend has been found for the produced H_2 mole fraction distribution, as shown in Fig. 15a and b, respectively. It should be noted that the H_2 mole fraction increases slowly along the main flow direction close to the exit of the longer reformer (see Fig. 15b), where the CH_4 fraction is zero in the corresponding regions as shown in Fig. 14b. That is due to the water gas-shift reaction in Eq. (2), by consuming CO and generating CH_4. It should be noted that water gas-shift reaction rate is small compared to other two reactions in Eqs. (1) and (3).

6. Conclusions

A fully three-dimensional calculation method has been further developed to simulate and analyze gas flow and heat transfer processes coupled by the chemical reactions in a composite duct relevant for a compact reformer. The model offers the possibilities of determining temperature and fuel gas species distribution profiles by taking into account the methane steam reforming, water gas-shift and reverse methanation reactions. It is found that the operating temperature and the catalyst loading significantly affect the transport processes and reforming reactions. Both higher temperature and larger catalyst loading promote faster reactions, i.e., bigger values of the maximum reaction rates appear within a thin porous region close to the interface between the fuel flow duct and the porous catalytic layer in the entrance region. For the base condition, the methane mass conversion efficiency at the exit of the fuel reforming duct reaches more than 95% at a larger catalyst loading (10 g_{cat}/cm^3) and higher operating temperature (700 °C). Sensitive studies are also conducted for various parameters relating to reformer configuration, such as reformer length and porous layer thickness, to reveal the importance of optimal duct design and configuration.

Acknowledgements

The Swedish Research Council (VR) and Sida Research Links programme supports the collaboration between Dalian Maritime University and Lund University.

References

[1] D.L. Hoang, S.H. Chan, Modeling of a catalytic autothermal methane reformer for fuel cell applications, Appl. Catal. A: Gen. 268 (2004) 207–216.
[2] I. Samanta, R.K. Shah, A. Wagner, Fuel processing for fuel cell application, Fuelcell2004-1515, in: R.K. Shah, S.G. Kandlikar (Eds.), Proceedings of Fuel Cell Science, Engineering and Technology, ASME, New York, 2004.
[3] R. Farrauto, S. Hwang, L. Shore, W. Ruettinger, J. Lampert, T. Giroux, Y. Liu, O. Ilinich, New material needs for hydrocarbon fuel processing: generating hydrogen for the PEM fuel cell, Ann. Rev. Mater. Res. 33 (2003) 1–27.
[4] A.L. Dicks, P. Goulding, S.L. Jones, R. Judd, K. Ponton, Assessment of advanced catalyst performance and fabrication options for a compact steam reformer, ETSU F/02/00180/REP, DTI PUB URN 01/1163, UK, 2001.
[5] M. Zanfir, A. Gavriilidis, Catalytic combustion assisted methane steam reforming in a catalytic plate reactor, Chem. Eng. Sci. 58 (2003) 3947–3960.
[6] D.W. Agar, Multifunctional reactors: old preconceptions and new dimensions, Chem. Eng. Sci. 54 (1999) 1299–1305.
[7] V.A. Kirillov, N.A. Kuzin, A.V. Kulikov, S.I. Fadeev, A.B. Shigarov, V.A. Sobyanin, Thermally coupled catalytic reactor for steam reforming of methane and liquid hydrocarbons: experiment and mathematical modeling, Theor. Found. Chem. Eng. 37 (2003) 276–284.
[8] J. Yuan, B. Sundén, A numerical investigation of heat transfer and gas flow in proton exchange membrane fuel cell ducts by a generalized extended darcy model, Int. J. Green Energy 1 (2004) 47–63.
[9] J. Yuan, M. Rokni, B. Sundén, Three-dimensional computational analysis of gas and heat transport phenomena in ducts relevant for anode-supported solid oxide fuel cells, Int. J. Heat Mass Transfer 46 (2003) 809–821.
[10] B.A. Haberman, J.B. Young, Three-dimensional simulation of chemically reacting gas flows in the porous support structure of an integrated-planar solid oxide fuel cell, Int. J. Heat Mass Transfer 47 (2004) 3617–3629.
[11] I.L. Mostinsky, Diffusion coefficient, in: G.F. Hewitt, G.L. Shires, Y.V. Polezhaev (Eds.), International Encyclopedia of Heat & Mass Transfer, CRC Press, FL, USA, 1996.
[12] S.S.E.H. Elnashaie, A.M. Adris, A.S. Al-ubaid, M.A. Soliman, On the non-monotonic behaviour of methane-steam reforming kinetics, Chem. Eng. Sci. 45 (1990) 491–501.
[13] J.R. Ferguson, J.M. Fiard, R. Herbin, Three-dimensional numerical simulation for various geometries of solid oxide fuel cells, J. Power Sources 58 (1996) 109–122.
[14] C.M. Rhie, W.L. Chow, Numerical study of the turbulent flow past an airfoil with trailing edge separation, AIAA J. 2 (1983) 1527–1532.
[15] B. Alazmi, K. Vafai, Analysis of fluid flow and heat transfer interfacial conditions between a porous medium and a fluid layer, Int. J. Heat Mass Transfer 44 (2001) 1735–1749.
[16] T. Ackmann, L.G.J. Haart, W. Lehnert, F. Thom, Modelling of mass and heat transport in thick-substrate thin-electrolyte layer SOFCs, in: Proc. 4th European Solid Oxide Fuel Cell Forum 2000, Lucerne/Switzerland, pp. 431–438.